Multimodal Nanoscale Tomographic Imaging for Battery Electrodes

Simon Müller[1], Manuel Lippuner[1], Mariana Verezhak[2], Vincent De Andrade[3], Francesco De Carlo[3], Vanessa Wood[1]

[1]Department of Information Technology and Electrical Engineering, ETH, Zurich 8092, Switzerland
[2]Paul Scherrer Institut, Forschungsstrasse 111, Villigen 5232, Switzerland
[3]Advanced Photon Source, Argonne National Laboratory, Lemont 60439, USA

Keywords*:*

Tomography, multimodal imaging, 3D microstructure, multiphase segmentation, composite electrode, carbon black binder domain, electrochemical simulation

Abstract

Accurate representations of the 3D structure within a lithium-ion battery are key to understanding performance limitations. However, obtaining exact reconstructions of electrodes, where the active particles, the carbon black and polymeric binder domain, and the pore space are visualized is challenging. Here, we show that multi-modal imaging can be used to overcome this challenge. We combine high-resolution ptychographic x-ray computed tomography with lower resolution but higher contrast transmission x-ray tomographic microscopy to obtain 3D reconstructions of pristine and cycled graphite-silicon composite electrodes. This cross-correlation enables quantitative analysis of the surface of active particles, including the heterogeneity of carbon-black and binder domain and solid-electrolyte interphase coverage. Capturing the active particles as well as the carbon-black binder domain allows using these segmented structures for electrochemical simulations to highlight the influence of the particle embedding on local state of charge heterogeneities.

Main Text

Introduction

The 3D structure within a lithium ion battery (LIB) has been shown to have an important impact on performance.[1] The structure of pore phase impacts the conductivity and diffusivity of lithium ions in the liquid electrolyte, limiting the charge and discharge times of a cell.[2] Particle size and shape determine the active material surface area and consequently the exchange current, which gives an upper limit to the applicable current rates.[3,4] Structure also influences the mechanical response of a system and, in combination with the elastic properties of the materials, determines how the material deforms or fractures during charge-dependent particle expansion and contraction.[5] Heterogeneity in structure properties leads to unevenly distributed local current loads and drives battery degradation and aging.[6] An accurate representation of the structure is therefore crucial to determine features that limit performance and to gain insight into possible design improvements.

One challenge in capturing the structure of a battery lies in the heterogeneity of the constituent materials, which includes ceramics, carbon compounds, polymers, metals, and liquids, as well as their diverse length scales and morphologies. The size of the active material particles typically ranges from hundreds of nanometers to tens of micrometers,[7] while the characteristic size of the conductive additives[8] and polymer binders is tens of nanometers. Additional challenges arise from chemically light materials that show low contrast with the pore space with attenuation-based x-ray and electron backscattered imaging techniques, and the combination of low contrast and small particle size is particularly unfavorable for accurate imaging.[9] Currently, there is no single imaging technique that accurately captures the active materials, the conductive additives and binder, and the pore-space in the battery simultaneously.

X-ray tomography (XTM)-based imaging has become established in the battery community to obtain 3D representations of battery structure.[10] XTM offers non-destructive and fast image acquisition combined with a spatial resolution in the submicron range. While this enables

reconstruction of the micron-sized active particles, imaging with voxel sizes of 10-20 nm, which is needed to resolve the carbon-black and binder domain (CBD), is possible but non-trivial. Focused-ion-beam scanning electron microscopy (FIB-SEM) provides higher resolution[11] and offers clear visual indications of the structural morphology at different length scales and thus is an ideal tool to investigate the CBD phase.[12] However, unlike XTM, it is a destructive procedure and requires sample infilling in order to get quantifiable and segmentable imaging data as empty pore space would lead to curtaining and depth artefacts.

Typically, 3D structures where the active particles, the conductive additives, binder, and the pore-space are present are investigated using correlative measurement techniques,[13,14] computer-generated material phases,[15] or (partial) substitution of the low-contrast carbon-black binder domain with more detectable substances.[16,17] Indeed, the high-resolution 3D reconstructions of battery electrodes typically suffer from one of two drawbacks: either (1) individual particles are recorded without the surrounding electrode structure,[18] or (2) the pore space of the sample is infilled with epoxy during sample preparation, which may destroy the fine features.[19,20]

Here, we show how these challenges can be overcome with advanced sample preparation and multimodal imaging. As a model system, we choose a high-energy negative electrode that presents the key imaging challenges found in battery electrodes – low contrast materials and materials with feature sizes spanning orders of magnitudes. We first describe how electrode samples that are not infilled can be prepared for nanoscale imaging using scanning laser milling. We then apply two different tomographic imaging techniques: first, ptychographic x-ray computed tomography (PXCT), providing high resolution to resolve the structures and second, transmission x-ray tomographic microscopy (TXTM), providing the contrast needed to distinguish the material composition - and merge the data sets using image registration protocols. The combined data sets can be used for new types of structural analysis and electrochemical simulation.

Sample Preparation for Imaging at the Nanoscale

To enable quantitative imaging of nanoscale features with x-rays, it is important to: (1) have small samples and (2) ensure that the internal structure of the sample is preserved during the sample preparation. High-resolution, quantitative x-ray tomography imaging requires a small sample diameter in order to avoid local tomography[21],[22] (e.g. artefacts and loss of quantitativeness of contrast that would result if the entire sample does not fit in the measurement field of view in case of PXCT or if the sample is larger than the depth of focus of the microscope for TXTM). At the same time, for an electrode with an average active particle size of 15 µm and a porosity between 30% and 40%,[23] the smallest representative cylindrical sample size is around 40 µm in diameter. Since porous samples easily break when mechanically milled to small dimensions, in previous tomographic imaging experiments, small electrode samples were in-filled to preserve their mechanical integrity. However, particularly, when imaging thin, web-like features, electrode infilling should be avoided since it is difficult to determine whether the introduction of the infilling phase impact the structure within the electrode.

To obtain small samples while preserving the mechanical integrity of sample and avoiding infilling, we use ultrashort pulsed solid-state lasering on a scanning system to mill the samples to the shape[24] shown in **Figure 1a**. Precise adjustment of the system parameters (e.g., laser wavelength and power, scanning speed, sample turning rate and most importantly the focus spot, see **Supplementary Information**) allows for reliable milling of heterogeneous samples consisting of metals, carbon compounds, polymers, and ceramics down to tens of microns without observable heat damage. The achieved sample diameter of below 40µm can potentially be further reduced without infilling of the sample required.

For this study, we select a graphite-silicon composite electrode as a model system since it contains relevant materials and the key imaging challenges found in battery electrodes: low contrast materials and small feature sizes.[25] The smallest feature size of carbon black and

chipped graphite flakes is in the nanometer range, and the different particle shapes lead to a heterogeneous structure. The graphite, the carbon-black and binder are carbon-based, which means their effective core charge number is small and similar. Accordingly, their signals are low and difficult to distinguish from one another. Furthermore, during cycling, a carbonous solid electrolyte interface (SEI) grows steadily on the silicon.[26]

Multimodal Nanoscale Imaging and Segmentation

To obtain 3D image data with sufficient resolution and sufficient contrast, we select two different techniques: ptychographic x-ray computed tomography (PXCT) for resolution and transmission x-ray tomographic microscopy (TXTM) for contrast. In post-processing, we register the two data sets to capture the desired information from each.

PXCT[27] combines scanning x-ray microscopy and coherent lensless imaging to computationally reconstruct 3D volumes with quantitative contrast. PXCT provides both phase and absorption contrast images, the former at hard x-ray photon energies offers significantly higher signal to noise ratio, and therefore higher resolution compared to the latter.[28] The achieved 20 nm voxel size and 40 nm spatial resolution allows clear discrimination between the pore-space and solids. In addition, features from the exact particle shapes to single carbon black particles or graphite flakes can be recognized (**Figure 1c**). Unfortunately, graphite and silicon particles have very similar electron densities and therefore cannot be distinguished with phase contrast only. Absorption tomograms acquired simultaneously could theoretically help to distinguish between these two phases; however, the low signal to noise ratio renders this almost impossible (see **Supplemental Information**).

Instead, to identify the different material phases, we turn to TXTM experiments. The 27.5 nm voxel size is slightly larger than in the PXCT measurement and the spatial resolution is significantly worse (~130 nm), but the variations in gray value, which come from the differences in attenuation, allow the different materials to be distinguished (**Figure 1b**).

Since the samples have been imaged at two different beamlines with different imaging techniques and unequal resolutions, an interactive image registration[29] is required. In a first step, we roughly manually align the two image stacks (e.g. in ImageJ). Then, iterative image registration is performed using elastix software.[30] Following an initial rigid transformation, the final non-rigid transform is applied.

The combined images contain the resolution of PXCT and contrast of TXTM (**Figure 1d**). This enables the mathematical identification and segmentation of the graphite and silicon active particles, the carbon-black and binder domain, pore space, and (for the cycled sample) the SEI based on thresholding and simple morphological operations. As a result, we get an accurate three-dimensional representation of the electrode sub-volume (**Figure 1f**).

Nanoscale Structural Analysis

The detailed structural information visible in PXCT reveals a wide range of particle features and shows the ramifications of battery cycling on the different material phases. **Figure 2a-c** show the details of graphite and silicon particles as well as their interconnections through the carbon-black and binder domain (CBD). **Figure 2d** shows an extract of a graphite particle taken from the cycled sample. Fractures orthogonal to the particle texture are visible, resulting from the mechanical forces during battery operation.[31,32] The silicon particle from the cycled sample (**Figure 2e**) is almost completely coated with a thin, heterogeneous SEI. **Figure 2f** shows that the SEI not only covers the silicon particles, but also clogs pores within the CBD.

Such high-resolution segmentations allow for quantitative analysis of interfaces and their evolution during cycling. Per imaged electrode, it is possible to assess the surface of approximately 90 silicon particles (**Figure 2g**). By implementing a ray-tracing algorithm (description in the **Supplemental Information**), we find that 53% of the pristine silicon particles surfaces is free (i.e. exposed to electrolyte) while 45% is covered by the carbon black and binder (i.e., where electron exchange to and from the particle will occur). The remaining

2% of the silicon particle surface is in intimate touch with other silicon or graphite particles. Following cycling, 53% of surfaces of the silicon particles are covered by the SEI. As can be seen in **Figure 2e** and **2f**, the SEI grows mainly on the previously free silicon surface, but also pushes away the CBD layer, which is now only in contact with 32% of the silicon surface. 14% of the silicon surfaces remain in contact with the pores. Such analysis enables the identification of CBD detachment from particles[33] that was not possible in three dimensions up to now.

The heterogeneity of the SEI thickness can also be quantified (**Figure 2i**). 50% of all silicon particles in the cycled sample have an average SEI thickness between 142 and 196 nm (**Figure 2h**), but some particles have average SEI thicknesses of up to 300 nm. For 50% of particles, the thickness of the SEI on the particles varies within a standard deviation of 60 nm to 115 nm, with the largest observed standard deviation of 200 nm. While measurements of more samples would be needed to improve the statistical significance of these results and reveal why the SEI thickness changes in different regions, this analysis shows that the SEI thickness varies across individual particles as well as among particles.

Simulating the Electrochemical Behavior

The uniqueness of the present dataset lies in its high spatial accuracy surpassed only by FIB SEM or TEM. However, as introductorily mentioned, quantitative FIB SEM would require infilling of the sample, which potentially destroys fine features, an aggravating circumstance especially when it comes to analyzing particle surfaces interfaces. TEM on the other hand misses the option to image a representative cut-out of an electrode with intact particle embeddings.

For these reasons, our obtained dataset is particularly attractive for studying the electrochemical behavior of single particles within their adjacent environment (i.e., as a function of the amount of CBD and SEI coverage).

The simulation environment and model are described in detail in the **Supplemental Information**. Ionic transfer is allowed over the free particle surface and electric transfer only takes place where the silicon particle is contacted by the CBD. The SEI is considered to be electronically insulating and its ionic conductivity is set to be thickness-dependent (with specific resistance increasing by a factor of 0.3 $\Omega cm^2/nm^{[34]}$). Charge and concentration gradients within the particle are subject to three-dimensional diffusion.

The first scenario looks at a silicon particle that is embedded in the center of the pristine electrode (**Figure 3a**). Starting from an initial state of charge (SOC) of 80%, the particle is delithiated with two current rates, 0.4 C and 1.2 C. Looking at the SOC distribution within the particle (**Figure 3b**), we find that tripling the c-rate from 0.4 to 1.2 leads to tripling the width of the 50% probability interval (**Figure 3c**) in the resulting SOC distribution in the silicon particle. It can be concluded that heterogeneities in SOC not only appear because of an inhomogeneous electrode structure but also on a particle level due to the asymmetric particle shape and the random embedding in the CBD. These inevitable heterogeneities are getting more pronounced as the applied c-rate, hence current, is increased.

In the second scenario (**Figure 3 d**), we investigate whether the particle is electronically or ionically limited during delithiation. The particle is delithiated from 6% SOC at different currents. For a lithiation of 5.5% and lower, the resulting Si-Li alloy does not have metallic characteristic, which means that the electrons cannot move freely. This leads to a gradient of electrons in the silicon particle in addition to the gradient in the SOC (**Figure 3e**). As shown in **Figure 3f**, the electric connection of the particles can provide a steady-state current-rate of up to 1.3 C whereas the steady state ionic current peaks at 0.9 C. This indicates that, for the case of silicon active particles, the lithiation and delithiation of the silicon are ionically limited until the particle detaches from the surrounding CBD matrix, which means that the particle becomes electric isolated.

The third scenario (**Figure 3g**) investigates the impact of the SEI during delithiation by comparing the same silicon particle with its actual SEI and with the SEI computationally removed. Starting from 80% SOC, the particle is delithiated with current rates from 1.1 C to 2.1 C. The presence of the SEI enhances the heterogeneous SOC distribution in the silicon particle (**Figure 3h**) and leads to larger overpotentials (**Figure 3i**). For a c-rate of 1.1, we find an overpotential of 20 mV without SEI and an overpotential of 30 mV with SEI. The difference in overpotential increases with increasing c-rates leading to an overpotential of 38 mV without SEI in contrast to 60 mV with SEI at 1.1 C (**Figure 3i**). This simulation highlights that heterogeneities in the SOC and overpotential caused by the SEI not only scale with the applied c-rate, but also become enhanced during battery operation as the SEI grows.

These simulations offer example use cases for high-resolution volumetric data and show that heterogeneities in lithium ion batteries originate not only from a heterogeneous microstructure[23], but already within individual active particle level due to the non-uniform CBD. Furthermore, heterogeneities are likely to get more pronounced as the electrode ages and the SEI grows, which leads to larger over-potentials and reduced usable capacity.

Conclusion

In summary, this work shows how a high-resolution imaging technique such as PXCT can be combined with a lower resolution technique that offers contrast to enable a semantic segmentation of the different materials. Here, the approach was used to resolve the features of pristine and cycled graphite-silicon electrodes, but this approach can be generally applied to combine multiple datasets with different resolutions and different information in the grayscale values.

While the complex sample preparation and lasering can be potentially circumvent in the future with ptychographyic X-ray laminography,[35] the long image acquiring time for the PXCT

impedes even higher resolution for a representative sample size and makes the realizability of in operando studies a tricky endeavor.

Careful selection of the techniques can be matched to the particular challenges of the sample of interest. Indeed, the demonstrated sample preparation, imaging, and registration techniques are by no means limited to lithium ion battery electrodes. These samples studied here present imaging challenges (i.e., low absorption contrast and feature sizes from microns to tens of nanometers) that can be found in many heterogeneous systems including solid state electrolyte batteries, gas diffusion layers of fuel cells, (super)capacitors, solar cells, and various biological specimens.

Specifically the improvement of solid state electrolyte batteries significantly relies on keeping an intact interface between particle and solid electrolyte,[36] a property the proposed methodology is predestinated to characterize, especially considering the wide variety of materials involved, ranging from chemically light lithium metal to heavier garnet types.[37] Furthermore, to additionally increase the electrolyte conductivity whilst providing the needed elasticity to maintain close contact to the active particles during battery operation, composite solid electrolytes consisting of a polymer matrix with incorporated ceramics[38] are in the ascendant. Such mixtures are hard to image with customarily techniques due to the low contrast of the polymer phase. The combination of PXCT and TXTM however is able to overcome these challenges.

Experimental Section

Electrode preparation. A silicon graphite composite electrode sheet with 30 wt.% silicon (BASF, SiOx, x≈1, 2275 mAh g−1), 55 wt.% graphite (Timcal Timrex SLP30), 10 wt.% polyvinyldiene difluoride (PVDF) binder (Kynar Flex® HSV900), and 5 wt.% carbon black (Timcal Super C60, Imerys) is prepared. For better imaging contrast, 50 vol. % of the carbon black in the carbon black-binder domain is substituted by carbon-coated copper nanoparticles

(US Research Nanomaterials Inc.). 13-mm disk-shaped electrodes are punched out from the electrode sheet, compressed with 900 kg, and transferred into an Argon-filled glovebox.

Half-cell cycling. A coin cell is assembled using lithium metal counter electrodes (Alfa Aesar, lithium foil, 99.9%), 500μl standard LP50 electrolyte (BASF, 1M LiPF6 in ethylene carbonate: ethyl methyl carbonate = 1:1 by weight), and a 250 μm thick glass fiber separator (Whatman® glass microfiber filter). The cell is operated galvanostatically at a C/30 rate between 10 mV and 1.5 V for 10 cycles using an MPG2 battery cycling system (Biologic). An additional 20 h potentiostatic step at 3 V is added at the end of the protocol to remove all lithium in the composite electrode. The electrochemical cycling data is shown in Supplementary Figure 1.

Sample preparation. The cycled electrode is rinsed with dimethyl carbonate (DMC) and subsequently dried.1-mm diameter disks are punched out of the pristine and the cycled electrode are glued onto OMNY pins.[39] The samples are laser milled to a diameter of below 40 μm at full electrode thickness of 65 μm.

Ptychographic x-ray computed tomography measurements and data processing. PXCT measurements are carried out at the cSAXS beamline of the Swiss Light Source (SLS) at the Paul Scherrer Institute, Villigen, Switzerland, using the flOMNI setup[40] with a beam energy of 6.2 keV and a Pilatus 2M detector placed 7.362 m downstream of the sample.
Ptychographic scans were performed with a 48 μm × 20 μm field of view. The scan points were positioned following a Fermat spiral trajectory[41] with a step size of 1.3 μm and an exposure time per point of 0.1 s. Ptychographic projections were reconstructed in an area of 400×400 pixels of the Pilatus detector, acquiring two detector positions to recover the information lost in the detector modules gaps, resulting in a voxel size of 21.4 nm using 800 iterations of the difference map (DM) algorithm[42] followed by 800 iterations of a maximum likelihood (ML) refinement[43] using cSAXS MATLAB code.

For tomography, 1644 projections (pristine sample) and 1303 projections (cycled sample) equally spaced over a 180-degree angular range were recorded which resulted in the total time of 55 h and 48 h per tomogram, respectively. The phase of the reconstructed projections was used after post-processing alignment and removal of constant and linear phase components, and a modified filtered back projection algorithm was applied for the tomographic reconstruction.[44,45] The 3D resolution, determined by Fourier shell correlation (FSC)[46] with the ½-bit threshold criterion was 40.15 nm for the pristine sample and 40.8 nm for the cycled sample.

Transmission x-ray tomographic microscopy measurements. Attenuation-based TXTM experiments are carried out at the 32-ID-C beamline of the Advanced Photon Source at the Argonne National Laboratory at a beam energy of 8.4 keV and 7.7 keV. For each tomographic scan, 1024 projections with an exposure time of 2 s (ca. 35 min per scan) are acquired with a 2448×2048 pixel detector, resulting in a voxel size of 27.5 nm. The objective lens used for the measurements was a Fresnel zone plate with 50nm outermost zone width leading to a maximum achievable imaging resolution of about 50nm. Low absorption contrast for the carbonous compounds and imaging artefacts lead to a 3D resolution of 135.03 nm for the pristine sample and 129.76 nm for the cycled sample determined by FSC according to the ½-bit threshold criterion.

Transmission x-ray tomographic microscopy data processing. The projection data are reconstructed with Filtered Back Projection (FBP) algorithm using the Astra-toolbox in MATLAB. Paganin phase retrieval was applied as a low pass filter with a refractive index parameter ratio of $\delta/\beta = 0.028$.

Image registration. For the pristine and the cycled sample, the PXCT dataset and the TXTM datasets are spatially aligned. Image registration is performed using the elastix software.

Following an initial rigid transformation, a non-rigid b-spline-transform is applied. The advanced mattes mutual information is used as metric.

Image segmentation. Data segmentation and evaluation of the surface coverage of the silicon particles including the analysis of the SEI layer is performed in MATLAB.

3D diffusion model. The three-dimensional diffusion model is implemented in MATLAB using the finite element method with von Neumann boundary conditions in combination with the partial differential equation toolbox.

3D renderings. Three-dimensional visualizations are assembled using arivis Vision4D and Siemens NX12.

Data availability. The collected and analyzed data for the present study are available from the corresponding author upon request.

References
[1]   B. T. Habte, F. Jiang, *Solid State Ionics* **2018**, *314*, 81.
[2]   B. Delattre, R. Amin, J. Sander, J. De Coninck, A. P. Tomsia, Y. M. Chiang, *J.*

Electrochem. Soc. **2018**, *165*, A388.

[3]   R. Tian, S. H. Park, P. J. King, G. Cunningham, J. Coelho, V. Nicolosi, J. N. Coleman, *Nat. Commun.* **2019**, *10*, DOI 10.1038/s41467-019-09792-9.

[4]   B. Kang, G. Ceder, *Nature* **2009**, *458*, 190.

[5]   T. W. Kwon, J. W. Choi, A. Coskun, *Chem. Soc. Rev.* **2018**, *47*, 2145.

[6]   R. Xu, Y. Yang, F. Yin, P. Liu, P. Cloetens, Y. Liu, F. Lin, K. Zhao, *J. Mech. Phys. Solids* **2019**, *129*, 160.

[7]   F. Yang, Y. Liu, S. K. Martha, Z. Wu, J. C. Andrews, G. E. Ice, P. Pianetta, J. Nanda, *Nano Lett.* **2014**, *14*, 4334.

[8]   J. Biscoe, B. E. Warren, *J. Appl. Phys.* **1942**, *13*, 364.

[9]   P. Pietsch, V. Wood, *Annu. Rev. Mater. Res* **2017**, DOI 10.1146/annurev-matsci-070616.

[10]   M. Ebner, D. W. Chung, R. E. García, V. Wood, *Adv. Energy Mater.* **2014**, *4*.

[11]   M. F. Lagadec, M. Ebner, R. Zahn, V. Wood, *J. Electrochem. Soc.* **2016**, *163*, A992.

[12]   M. Shaibani, M. S. Mirshekarloo, R. Singh, C. D. Easton, M. C. Dilusha Cooray, N. Eshraghi, T. Abendroth, S. Dörfler, H. Althues, S. Kaskel, A. F. Hollenkamp, M. R. Hill, M. Majumder, *Sci. Adv.* **2020**, *6*, DOI 10.1126/sciadv.aay2757.

[13]   L. Zielke, T. Hutzenlaub, D. R. Wheeler, C. W. Chao, I. Manke, A. Hilger, N. Paust, R. Zengerle, S. Thiele, *Adv. Energy Mater.* **2015**, *5*, 1.

[14]   R. Moroni, M. Börner, L. Zielke, M. Schroeder, S. Nowak, M. Winter, I. Manke, R. Zengerle, S. Thiele, *Sci. Rep.* **2016**, *6*, 30109.

[15]   L. Zielke, T. Hutzenlaub, D. R. Wheeler, I. Manke, T. Arlt, N. Paust, R. Zengerle, S. Thiele, *Adv. Energy Mater.* **2014**, *4*, 2.

[16]   S. L. Morelly, J. Gelb, F. Iacoviello, P. R. Shearing, S. J. Harris, N. J. Alvarez, M. H. Tang, *ACS Appl. Energy Mater.* **2018**, *1*, 4479.

[17]   F. Tariq, V. Yufit, M. Kishimoto, P. R. Shearing, S. Menkin, D. Golodnitsky, J. Gelb, E. Peled, N. P. Brandon, *J. Power Sources* **2014**, *248*, 1014.

[18]   E. H. R. Tsai, J. Billaud, D. F. Sanchez, J. Ihli, M. Odstrčil, M. Holler, D. Grolimund, C. Villevieille, M. Guizar-Sicairos, *iScience* **2019**, *11*, 356.

[19]   S. Vierrath, L. Zielke, R. Moroni, A. Mondon, D. R. Wheeler, R. Zengerle, S. Thiele, *Electrochem. commun.* **2015**, *60*, 176.

[20]   Z. Liu, Y. C. K. Chen-Wiegart, J. Wang, S. A. Barnett, K. T. Faber, **2016**, 140.

[21]   P. Paleo, A. Mirone, *Adv. Struct. Chem. Imaging* **2017**, *3*, 1.

[22]   P. Paleo, M. Desvignes, A. Mirone, *J. Synchrotron Radiat.* **2017**, *24*, 257.

[23]   S. Müller, J. Eller, M. Ebner, C. Burns, J. Dahn, V. Wood, *J. Electrochem. Soc.* **2018**, *165*, A339.

[24]   J. J. Bailey, T. M. M. Heenan, D. P. Finegan, X. Lu, S. R. Daemi, F. Iacoviello, N. R. Backeberg, O. O. Taiwo, D. J. L. Brett, A. Atkinson, P. R. Shearing, *J. Microsc.* **2017**, *267*, 384.

[25]   D. Leanza, C. A. F. Vaz, I. Czekaj, P. Novak, M. El Kazzi, *J. Mater. Chem. A* **2018**, 3534.

[26]   E. Peled, S. Menkin, *J. Electrochem. Soc.* **2017**, *164*, A1703.

[27]   M. Holler, A. Diaz, M. Guizar-Sicairos, P. Karvinen, E. Färm, E. Härkönen, M. Ritala, A. Menzel, J. Raabe, O. Bunk, *Sci. Rep.* **2014**, *4*, 1.

[28]   M. Dierolf, A. Menzel, P. Thibault, P. Schneider, C. M. Kewish, R. Wepf, O. Bunk, F. Pfeiffer, *Nature* **2010**, *467*, 436.

[29]   D. Shamonin, *Front. Neuroinform.* **2014**, *7*, 1.

[30]   S. Klein, M. Staring, K. Murphy, M. a. Viergever, J. Pluim, *IEEE Trans. Med. Imaging* **2010**, *29*, 196.

[31]   J. Cannarella, C. B. Arnold, *J. Power Sources* **2014**, *245*, 745.

[32]   W. Li, Y. Xia, J. Zhu, H. Luo, *J. Electrochem. Soc.* **2018**, *165*, A1537.

[33] S. Müller, P. Pietsch, B.-E. Brandt, P. Baade, V. De Andrade, F. De Carlo, V. Wood, V. Nardone, E. Parisini, *Nat. Commun.* **2018**, *9*, 1.

[34] T. Swamy, Y. M. Chiang, *J. Electrochem. Soc.* **2015**, *162*, A7129.

[35] M. Holler, M. Odstrcil, M. Guizar-Sicairos, M. Lebugle, E. Müller, S. Finizio, G. Tinti, C. David, J. Zusman, W. Unglaub, O. Bunk, J. Raabe, A. F. J. Levi, G. Aeppli, *Nat. Electron.* **2019**, *2*, 464.

[36] J. Janek, W. G. Zeier, *Nat. Energy* **2016**, *1*, 1.

[37] Z. Gao, H. Sun, L. Fu, F. Ye, Y. Zhang, W. Luo, Y. Huang, *Adv. Mater.* **2018**, *30*, 1.

[38] Z. Li, H. M. Huang, J. K. Zhu, J. F. Wu, H. Yang, L. Wei, X. Guo, *ACS Appl. Mater. Interfaces* **2019**, *11*, 784.

[39] M. Holler, J. Raabe, R. Wepf, S. H. Shahmoradian, A. Diaz, B. Sarafimov, T. Lachat, H. Walther, M. Vitins, *Rev. Sci. Instrum.* **2017**, *88*, DOI 10.1063/1.4996092.

[40] M. Holler, J. Raabe, A. Diaz, M. Guizar-Sicairos, C. Quitmann, A. Menzel, O. Bunk, *Rev. Sci. Instrum.* **2012**, *83*, DOI 10.1063/1.4737624.

[41] X. Huang, H. Yan, R. Harder, Y. Hwu, I. K. Robinson, Y. S. Chu, *Opt. Express* **2014**, *22*, 12634.

[42] P. Thibault, M. Dierolf, O. Bunk, A. Menzel, F. Pfeiffer, *Ultramicroscopy* **2009**, *109*, 338.

[43] P. Thibault, M. Guizar-Sicairos, *New J. Phys.* **2012**, *14*, DOI 10.1088/1367-2630/14/6/063004.

[44] M. Guizar-Sicairos, A. Diaz, M. Holler, M. S. Lucas, A. Menzel, R. A. Wepf, O. Bunk, *Opt. Express* **2011**, *19*, 21345.

[45] M. Guizar-Sicairos, J. J. Boon, K. Mader, A. Diaz, A. Menzel, O. Bunk, *Optica* **2015**, *2*, 259.

[46] M. Van Heel, M. Schatz, *J. Struct. Biol.* **2005**, *151*, 250.

Author contributions

S.M. performed the electrochemical cycling experiments and prepared the samples for the imaging campaign. S.M. and M.V conducted the PXCT imaging. S.M. and V.D.A. conducted the TXTM experiments. S.M. performed the registration, segmentation, and analysis of the image data. M.L built the MATLAB model. M.L. and S.M. analyzed the simulation results. S.M. and V.W. wrote the manuscript. All authors contributed to scientific discussions.

Additional information

Supplementary Information accompanies this paper at XXX

Competing interests: The authors declare no competing interests.

Reprints and permission information is available online at XXX
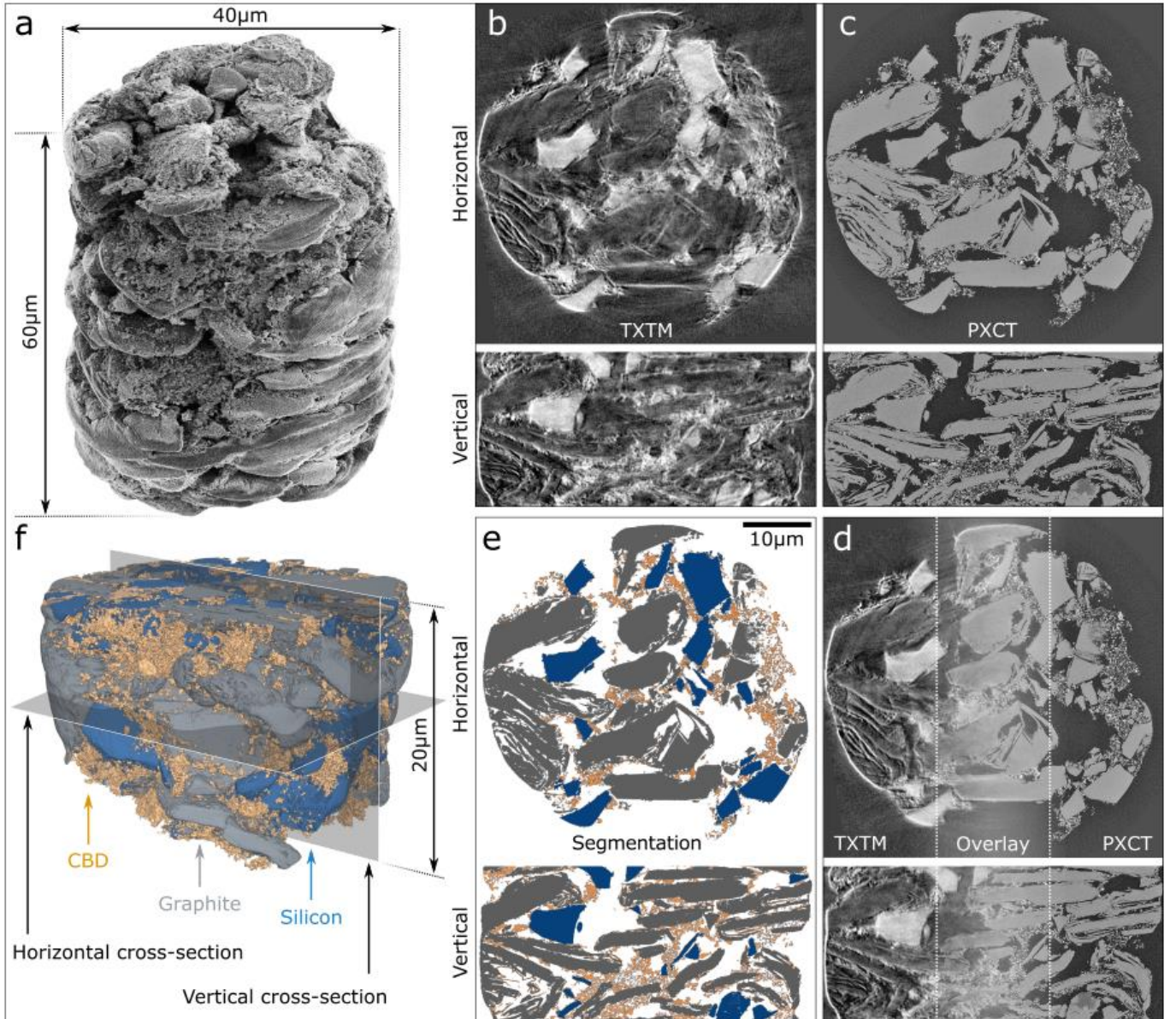
Figure 1: (**a**) Scanning electron microscope image of the laser milled sample used for ptychographic x-ray computed tomography and transmission x-ray tomographic microscopy. Cross-sections of the (**b**) transmission x-ray tomographic microscopy and (**c**) ptychographic x-ray computed tomography data. Overlay of the two data sets (**d**), and multi-phase segmentation showing graphite particles in gray, silicon particles in blue, and the CBD in orange (**e**). The same color code is used for the 3D representation of the electrode (**f**).
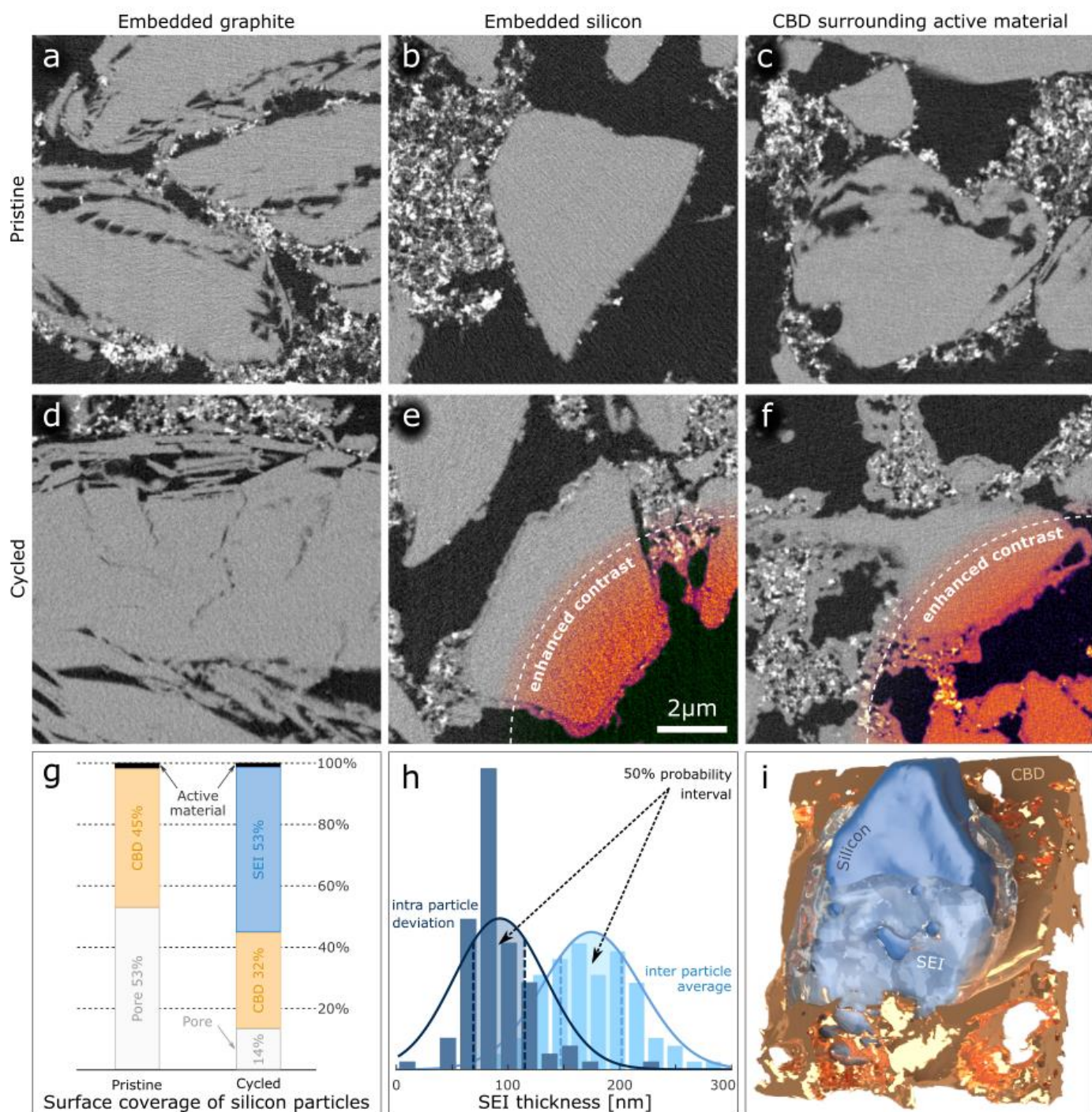
Figure 2: PXCT tomograms featuring (**a**) a graphite particle, (**b**) a silicon particle, and (**c**) the carbon-black binder domain between particles in the pristine sample. PXCT featuring (**d**) a graphite particle, (**e**) a silicon particle, and (**f**) the carbon-black binder domain between particles in the cycled sample. (**g**) The percentage surface coverage of the silicon particles in the pristine and cycled sample. (**h**) Distributions of the average SEI thickness of the cycled silicon particles (light blue) and the standard deviation of the SEI thickness per particle (dark blue). (**i**) 3D

rendering of a subvolume of cycled electrode showing a silicon particle (dark blue), the SEI (transparent), and the CBD (orange).
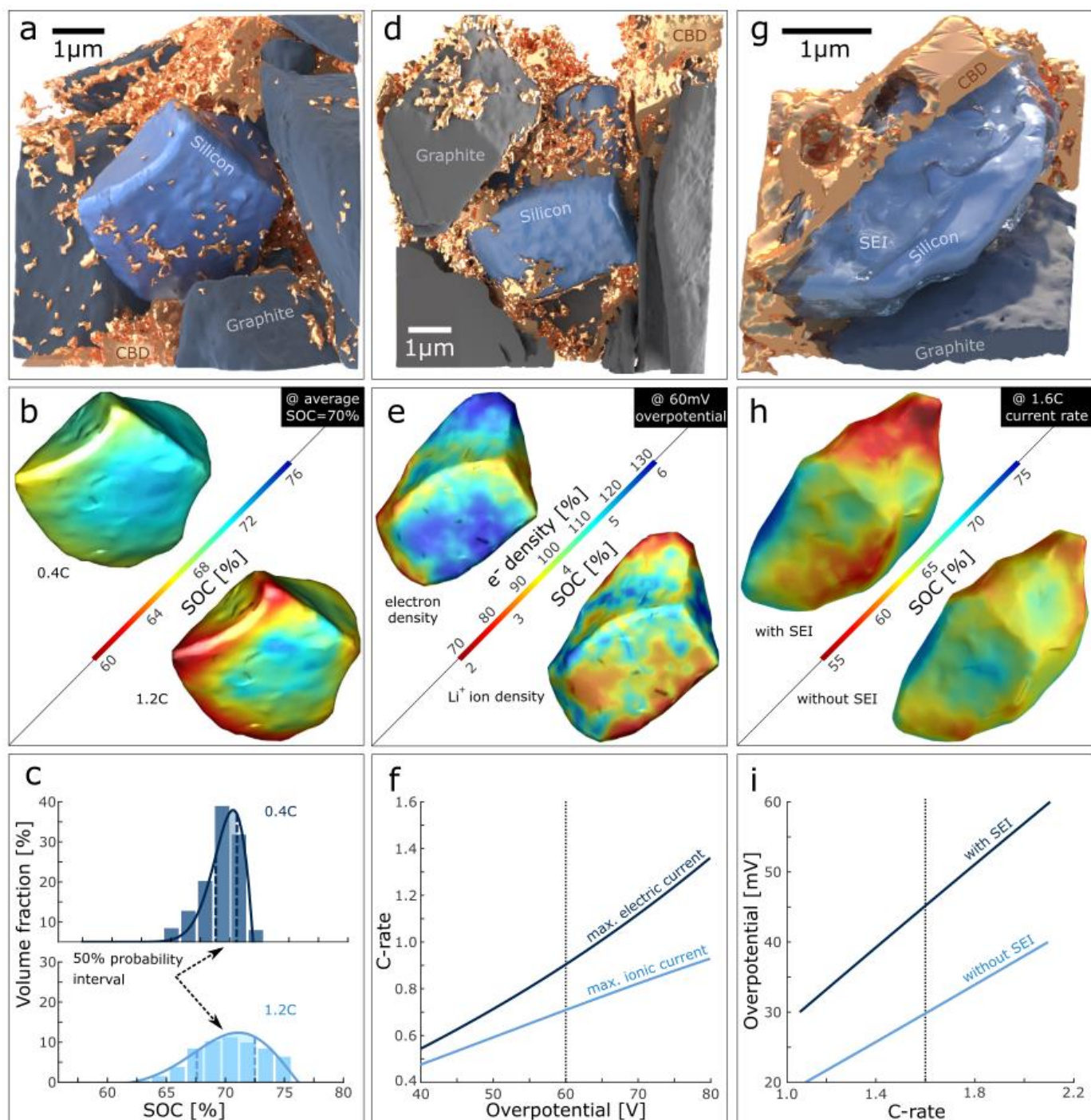
Figure 3 (a) A 3D rendering of a silicon particle and its surrounding from the pristine sample.
(**b**) State-of-charge (SOC) distribution within the silicon particle when the entire particle has
an average SOC of 70% for a current rate of 0.4 C (top) and 1.2 C (bottom). (**c**) The probability
distribution showing this SOC distribution in the two cases. (**d**) Another silicon particle
embedded in the microstructure of the pristine sample. (**e**) Electron (top) and Li distributions
(bottom) at an average SOC of 5.5% during delithiation. (**f**) The overpotential versus the current

rate of electronic and ionic currents. **(g)** A 3D rendering of a silicon particle and its surrounding from the cycled sample, showing an SEI. (**h**) SOC distribution within the silicon particle when the entire particle has an average SOC of 70% with its actual SEI (top) and in the case the particle would have no SEI (bottom). (**i**) The overpotentials as a function of current rate in the case the particle would have no SEI and with its actual SEI.